A Novel Strategy Based on Linear Active Disturbance Rejection Control for Harmonic Detection and Compensation in Low Voltage AC Microgrid

Hui Li [1], Shuang Li [1], Junwei Lu [2,*] and Yue Qu [1] and Chenmu Guo [1]

[1] College of Automation Engineering, Shanghai University of Electric Power, Shanghai 200090, China; lihui@shiep.edu.cn (H.L.); lsshdl@mail.shiep.edu.cn (S.L.); siachu@mail.shiep.edu.cn (Y.Q.); gcm1005@mail.shiep.edu.cn (C.G.)

[2] School of Engineering and Built Environment, Griffith University, Gold Coast, QLD 4222, Australia

* Correspondence: j.lu@griffith.edu.au; Tel.: +61-07-5552-7596

check for updates

Abstract: In an AC microgrid, harmonic distortion is mainly caused by power electronic equipment and nonlinear loads. In this paper, linear active disturbance rejection control (LADRC) is used to control the fundamental current at the point of common coupling (PCC). Meanwhile, an active power filter (APF) is added to eliminate the harmonic current generated by the nonlinear loads. The tracking differentiator (TD) in active disturbance rejection control (ADRC) serves as a low-pass filter (LPF) in the harmonic detection algorithm of APF. Compared to traditional harmonic detection algorithms, the improved strategy solves the contradiction between rapidity, accuracy, and overshoot of filtering. LADRC has good performance of disturbance rejection, internal decoupling, and accessible parameters tuning. It can observe the internal uncertainty and external disturbance of the system as the total disturbance through the extended state observer (ESO), and compensate it in time through state feedback to make the system achieve the desired performance. The abilities of resonance suppression for LCL-type filter and internal decoupling of LADRC demonstrates its advantages through frequency domain analysis and simulation. The proposed strategy was simulated in MATLAB/SIMULINK and realized in the experimental hardware platform, and the effectiveness of the proposed strategy is approved.

Keywords: LADRC; TD; harmonic detection and compensation; LPF

1. Introduction

With the continuous improvement of semiconductor manufacturing technology, the performance of power electronic devices has been strengthened. The grid-connected inverter as an energy conversion interface plays a crucial role in delivering high-quality power into the grid.

At present, a single-function inverter cannot meet the needs of modern power equipment, and it is necessary to design a system that can control the current at point of common coupling (PCC) and suppress the harmonics of the grid. Single-function systems are slowly evolving toward large-scale composite systems [1]. The grid-connected inverter is the critical equipment for grid-connected power generation of renewable energy. Compared with the L-type filter, the LCL-type filter has higher frequency harmonic suppression capability and smaller inductance, which can reduce the physical size [2,3].

The design of the LCL-type grid-connected inverter control system is generally based on the α-β stationary coordinate system and the d-q rotating coordinate system. In [4], the deadbeat control is proposed. The current control in the time domain is obtained by inverting the model according to the expected value of the controlled current at the next moment. The system response is faster but it

depends on the accurate modeling of the system. In [5], a model-predictive control (MPC) is proposed, which is based on the inequality constraints and objectives established by the precise mathematical model of the controlled object. It has satisfactory control performance, but the calculation amount is large, which is suitable for slow process control. Proportional resonance control (PR) is proposed in [6–8]. Its greatest characteristic is that it can obtain infinite gain at a certain frequency to realize the static error-free tracking of AC signal, but the disturbance rejection ability of the controller is poor.

Compared with the control strategies under the *abc* static coordinate system, in the *d-q* rotating coordinate system, the independent control of the active and reactive power current can be realized, and become the mainstream method of the grid-connected current control [9,10]. However, there is a coupling problem between *d*-axis and *q*-axis current. In [11,12], the LCL-type filter is equivalent to the L-type filter, which only decouples the filter inductance and ignores the coupling effect of the filter capacitance. In [13], the coupling problem is solved by controlling the inverter-side current. However, there is a phase difference between the output current and grid voltage. In [14], the feedback linearization theory is applied to the L-type and LCL-type inverters for the decoupling design. The decoupling ability depends on the accurate modeling of the system. In [15], a strategy based on the decoupling of feedforward is proposed. The coupling components of the same axis and the opposite directions are added to each axis to eliminate the coupling relationship between the *d*-axis and *q*-axis. In [16], a three-closed-loop decoupling control strategy is proposed, which uses dynamic feedback based on dual inductance current and capacitance voltage to realize dynamic decoupling of multi-input and multi-output linear time-invariant systems. The core idea of active disturbance rejection control (ADRC) proposed in [17] is to regard the uncertainty, model error and external disturbance in the system as an extended state, and the real-time estimation and compensation by the extended state observer (ESO). Hence, ADRC does not rely on accurate mathematical models, so it has a strong robustness and disturbance rejection ability. However, the construction of nonlinear functions and complex parameters tuning limits the widespread use of nonlinear ADRC in industry. To this end, ADRC has been simplified to linear form (LADRC) in [18] and has been used in power systems and power electronics [19–21].

The above method only considers that current distortion is not severe, but most of the loads are nonlinear in practical production. If grid-connected current control strategy is used in the power system without harmonic suppression, the power quality at PCC will not meet the standards set by the International Electrotechnical Commission (IEC). An active power filter (APF) is a more advanced power electronics device that compensates for harmonics today. Its good real-time performance and high compensation accuracy are gradually replacing passive power filters (PPF) [22–24]. The accuracy detection of harmonic current has a significant influence on the operation of the active power filter. If the harmonic current cannot be obtained accurately and in time, the APF cannot accurately compensate for the harmonic components. In [25], the author proposes an FFT-based harmonic detection method. The method requires two FFT transformations for harmonic detection, which reduces real-time detection. Besides, when the voltage waveform is changed, a large asynchronous sampling error will be caused, which will affect the detection accuracy of higher order harmonics. In [26], the author proposes a harmonic current detection method based on Fryze traditional power definition, which decomposes power into active power and generalized reactive power. This method is computationally intensive and causes large time delays. Wavelet analysis [27] overcomes the shortcomings of Fourier analysis in the frequency domain and no locality in the time domain. It can decompose the mixed signals of different frequency components into signal blocks of different frequencies to realize harmonic current detection. However, the wavelet transform is prone to aliasing, which reduces the detection accuracy.

According to the instantaneous reactive power theory proposed by H. Akagi [28], the *p-q* method, the *d-q* method, and the *ip-iq* method are proposed. In [29], the *p-q* method is proposed based on the instantaneous reactive power, and the harmonic current is calculated by the instantaneous active power and reactive power. This method has a fast detection speed and realizes a reactive

power compensation and harmonics compensation, but if the grid voltage is distorted, the detection is inaccurate. In [30], the *ip-iq* method is proposed, which can accurately detect the harmonic value of the symmetrical three-phase circuit, and has good real-time performance. When only harmonics are detected, the phase-locked loop (PLL) circuit can be omitted and adapted. In the case of asymmetric grid and voltage waveform distortion, since only $\sin \omega t$ and $\cos \omega t$ are operated in the *ip-iq* detection algorithm, the harmonic component of the distortion voltage does not appear in operation, so the harmonic current can also be accurately detected under the condition of the power supply voltage distortion, but the *p-q* method has a large error in this case. In [31], a harmonic detection method based on the generalized synchronous rotating frame system is proposed. Firstly, the three-phase current is transformed into the *d-q* coordinate system rotating at the k-th harmonic angular frequency, and then the low-pass filter is used to the DC component is filtered out, and then the *d-q* to *abc* inverse coordinate transformation is performed to obtain the k-th harmonic current to be detected. In this paper, an improved *ip-iq* harmonic algorithm is proposed. In the harmonic detection algorithm, a tracking differentiator (TD) is used instead of a Butterworth filter, which improves the detection speed and accuracy of the algorithm and solves the contradiction between overshoot and rapidity.

According to the requirements of grid-connected current power quality, this paper proposes a strategy with grid-connected current control and harmonic suppression. The structure of this paper is as follows: Section 2 is the mathematical model of the grid-connected inverter; Section 3 is the LADRC controller design; Section 4 is the frequency domain analysis of LADRC controller; Section 5 is the proposal and analysis of the harmonic detection method; Sections 6 and 7 are for simulation verification and physical experiment verification. Further discussion is given in Section 8. Finally, the experimental conclusions are given in Section 9.

2. System Characteristic Analysis

Grid-Connected Inverter Model Analysis

Traditional control strategies need to establish an accurate mathematical model of the object, whereas the uncertainties and external disturbances can not be built into the mathematical model, as it results in poor performance of the controller. The ADRC theory proposed by Jingqing Han is independent of any existing control theory. It can extract the total disturbance (internal uncertainty and external disturbance) of the system based on the input and output without an accurate mathematical model.

In this paper, an LCL-type grid-connected inverter with LADRC algorithm is used to control the amplitude and phase of the fundamental current at PCC, and APF is used to compensate harmonic current. Figure 1a depicts the circuit topology and control strategy of LCL-type grid-connected inverter and APF. The LCL filter consists of a converter-side inductance L_1, passive damping resistance R_d, filter capacitor C, and grid-side inductance L_2. R_d is passive damping resistance which is used to suppress the resonance of the LCL filter. In Figure 1b, ω_g is the grid voltage angular frequency. The PCC current is transformed from the *abc* stationary coordinate system to the *d-q* rotating system through the $\mathbf{C_{32}}$ transformation matrix. LESO is a state observer that estimates the system state variables, their differential signals, and the total disturbance of the system through the inputs and outputs of the system. z_{1dq} is the estimated value of i'_{2dq}, z_{2dq} is the differential signal of z_{1dq}, and z_{3dq} is the total disturbance of the system including internal disturbance and external disturbance. Controller 1 and Controller 2 are PD controllers, and the controller's output and total disturbance are subtracted to eliminate the total disturbance of the system. b_0 is the input gain of the system. The reference voltage signal of the inverter is then obtained by the $\mathbf{C_{23}}$ inverse transform matrix.

(a) Circuit topology of the composited system

(b) Grid-connected inverter control strategy

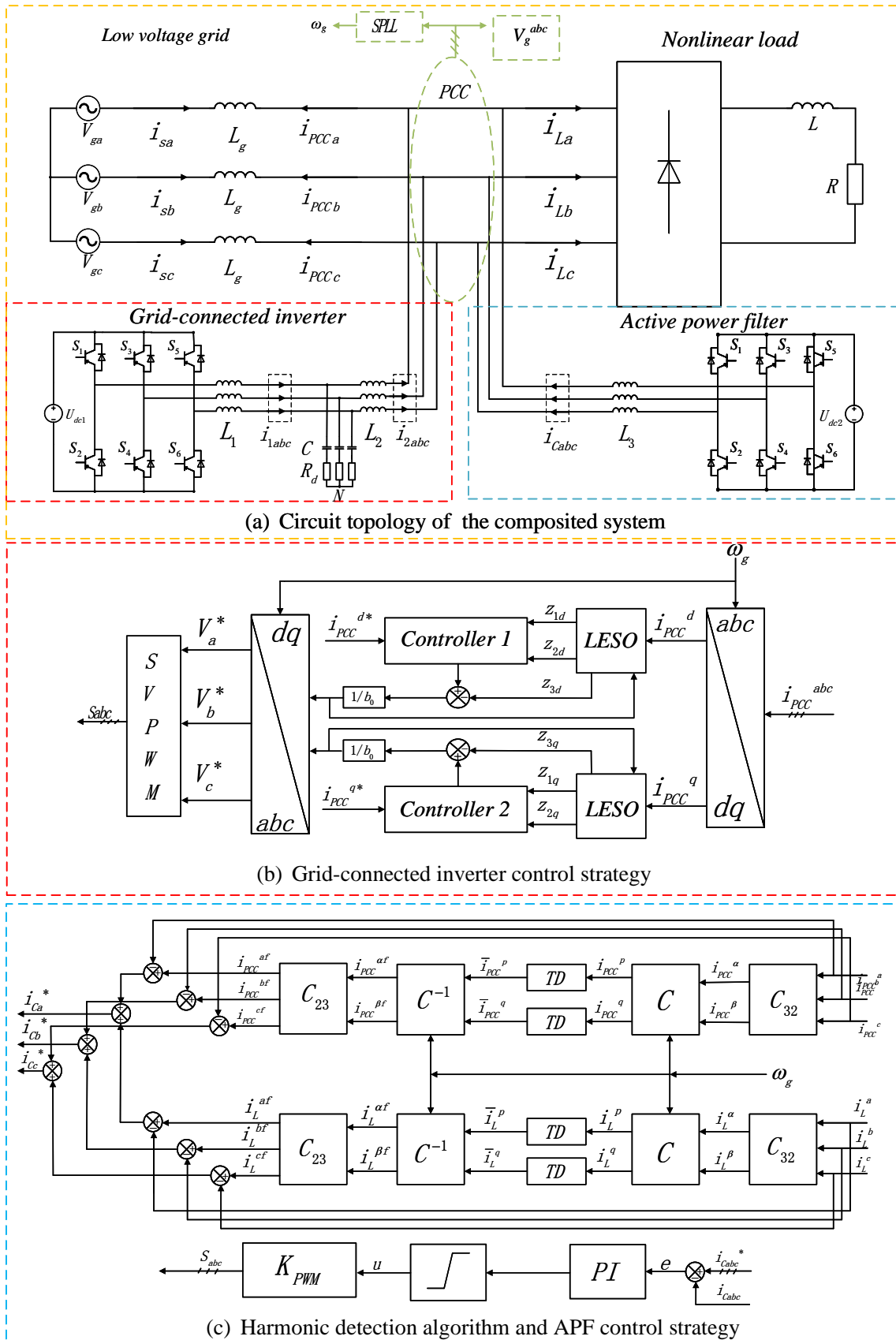(c) Harmonic detection algorithm and APF control strategy

Figure 1. Circuit topology and control strategy of LCL-type grid-connected inverter and an active power filter (APF).

In Figure 1c, the PCC current is transformed from the *abc* stationary coordinate system to the *α-β* stationary coordinate system by the transformation matrix $\mathbf{C_{32}}$. The transformation matrix $\mathbf{C}$ is transformed from the *α-β* coordinate system to the *d-q* rotation coordinate system. The fundamental component is converted into a DC component, and the other components are all AC components. The positive sequence component changes from kth to (k − 1)th, and the negative sequence component changes from kth to (k + 1)th. The DC component is obtained by filtering the AC component quickly by TD without overshoot. By transforming the matrices $\mathbf{C^{-1}}$ and $\mathbf{C_{23}}$, the *d*-axis component and the *q*-axis component are inversely transformed to the abc coordinate system to obtain the fundamental component of the current. The DC component and the PCC current are subtracted to obtain the harmonic command current. Harmonic compensation can be achieved by tracking the command current through the PI controller.

Complex space vectors in *d-q* coordinate system are implemented ($i_2 = i_{2d} + ji_{2q}$). Therefore, the state space expression of the LCL-type inverter is expressed in *d-q* coordinate system as:

$$\begin{cases} \dot{x}_{dq} = \mathbf{A}x_{dq} + \mathbf{B}K_{pwm}u_{idq} + \mathbf{F}v_{gdq}, \\ y = \mathbf{C}x_{dq}. \end{cases} \tag{1}$$

where, $x_{dq} = [i_{1dq}, i_{2dq}, v_{Cdq}]^T = [i_{1d} + ji_{1q}, i_{2d} + ji_{2q}, v_{Cd} + jv_{Cq}]^T$, i_{1dq} is the converter-side inductance current, i_{2dq} is the grid-side inductance current, v_{Cdq} is the capacitance voltage, K_{pwm} is the pulse width modulation gain, u_{idq} is the converter output voltage, and v_{gdq} is the voltage of the grid. For the convenience of analysis, make $K_{pwm} = 1$. All the above variables are state variables in the *d-q* coordinate system. The matrix in Formula (1) is represented as follows:

$$\mathbf{A} = \begin{pmatrix} -(\frac{R_d}{L_1} + j\omega_g) & \frac{R_d}{L_1} & \frac{1}{L_1} \\ \frac{R_d}{L_2} & -(\frac{R_d}{L_2} + j\omega_g) & \frac{1}{L_2} \\ \frac{1}{C} & -\frac{1}{C} & -j\omega_g \end{pmatrix}, \mathbf{B} = \begin{pmatrix} \frac{1}{L_1} & 0 & 0 \end{pmatrix}^T,$$

$$\mathbf{F} = \begin{pmatrix} 0 & -\frac{1}{L_2} & 0 \end{pmatrix}^T, \mathbf{C} = \begin{pmatrix} 0 & 1 & 0 \end{pmatrix}. \tag{2}$$

where, $\mathbf{A}$ is a system matrix whose parameters depend on the circuit components. $\mathbf{B}$ is the input matrix. $\mathbf{F}$ is the perturbation matrix. $\mathbf{C}$ is the output matrix.

The transfer function from input voltage $U_{idq}(s)$ to output current $I_{2dq}(s)$ is expressed as:

$$G_1(s) = \mathbf{C}(s\mathbf{I} - \mathbf{A})^{-1}\mathbf{B} = \frac{1}{L_1CL_2} \cdot \frac{1}{(s + j\omega_g)^3 + CR_dw_{res}^2(s + j\omega_g)^2 + w_{res}^2(s + j\omega_g)}. \tag{3}$$

The transfer function from grid disturbance $V_{gdq}(s)$ to output current $I_{2dq}(s)$ is expressed as:

$$G_2(s) = \mathbf{C}(s\mathbf{I} - \mathbf{A})^{-1}\mathbf{F} = \frac{1}{L_1CL_2} \cdot \frac{L_1C(s + j\omega_g)^2 + CR_d(s + j\omega_g) + 1}{(s + j\omega_g)^3 + CR_dw_{res}^2(s + j\omega_g)^2 + w_{res}^2(s + j\omega_g)}. \tag{4}$$

where w_{res} is the resonant frequency, and $w_{res}^2 = (L_1 + L_2)/(L_1CL_2)$. According to the above Formulas (1) and (2), the block diagram of the grid-connected inverter in the *s*-domain redefine the state variables, as shown in Figure 2.

According to Formulas (1) and (2), the control system model is a third-order system. Controller design only depends on the relative-order of the object, not the actual-order. The relative-order is equal to the number of minimum integrators passing through the input to the output path. It is not important whether the information transformation relationship between the integrators is linear or nonlinear, time-variant or time-invariant. In contrast, it is important that there is no information channel between the integrators. In the LCL-type filter with passive damping resistance, the passive damping resistance provides an information channel, so the shortest path passes through two integrators.

Therefore, according to Figure 2, the relative order of the LCL-type filter with passive damping resistance is two order.
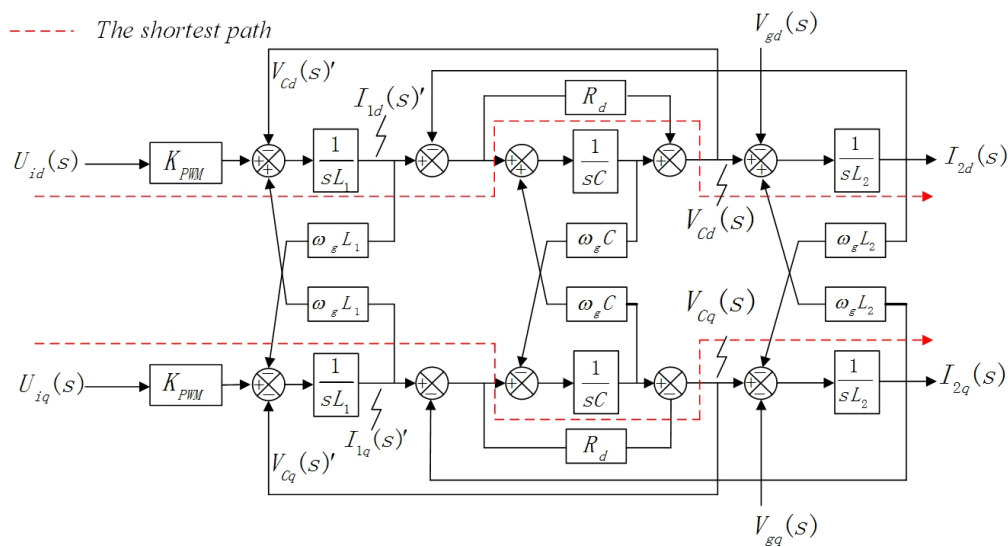

Figure 2. Block diagram of LCL-type filter with passive damping resistance.

The common method for judging the relative order is to establish an input–output equation, and the two sides of the equation are simultaneously differentiated. When an input item appears on the right side of the equation, the number of derivatives of the output is recorded as a relative order. The controller designed is a second-order LADRC controller with a third-order ESO.

According to the above block diagram, we redefine the state variables as shown in Figure 2.

$$
\begin{cases}
I'_{1d}(s) = I_{1d}(s), \\
I'_{2d}(s) = I_{2d}(s), \\
V'_{cd}(s) = V_{cd}(s) + R_d(I_{1d}(s) + I_{2d}(s)),
\end{cases}
\tag{5}
$$

where, $I'_{1dq}(s)$, $I'_{2dq}(s)$, $V'_{cdq}(s)$ are the newly defined state variable. The differential equation between input and output is shown as Formula (6).

$$
\begin{cases}
\dfrac{d^2 i'_{2d}}{dt^2} = b_0 u_{id} + f_d, \\
\dfrac{d^2 i'_{2q}}{dt^2} = b_0 u_{iq} + f_q,
\end{cases}
\tag{6}
$$

where,

$$
b_0 = \frac{R_d}{L_1 L_2}, f_d = f'_d + f'_{0d}, f_q = f'_q + f'_{0q},
$$

f_d and f_q are described as total disturbance that includes external disturbance and internal disturbance, i.e., v_{gd} grid voltage change, and internal dynamics, coupling term between d-axis and q-axis, and parameters variation. f'_{0d} and f'_{0q} are the part of the total disturbance that is known by modeling.

According to the above Formula (5), the system becomes a second-order system.

$$
\begin{cases}
f'_{0d} = -\dfrac{1}{L_2 C} i'_{2d}, \\[2mm]
f'_{0q} = -\dfrac{1}{L_2 C} i'_{2q}, \\[2mm]
f_d = -\dfrac{1}{L_2 C} i'_{2d} + \omega_g \dfrac{di'_{2q}}{dt} + \dfrac{1}{L_2 C} i'_{1d} + \dfrac{1}{L_2} \omega_g v'_{cq} \\[2mm]
\qquad - \dfrac{R_d}{L_1 L_2} v'_{cq} - \dfrac{R_d}{L_2^2} v'_{cd} - \dfrac{R_d}{L_2^2} v_{gd} - \dfrac{1}{L_2} \dfrac{dv_{gd}}{dt}, \\[2mm]
f_q = -\dfrac{1}{L_2 C} i'_{2q} - \omega_g \dfrac{di'_{2d}}{dt} + \dfrac{1}{L_2 C} i'_{1q} - \dfrac{1}{L_2} \omega_g v'_{cd} \\[2mm]
\qquad - \dfrac{R_d}{L_1 L_2} v'_{cd} - \dfrac{R_d}{L_2^2} v'_{cq} - \dfrac{R_d}{L_2^2} v_{gq} - \dfrac{1}{L_2} \dfrac{dv_{gq}}{dt}.
\end{cases}
\tag{7}
$$

According to Formula (7), it can be found that the LCL-type filter is a multivariable, strongly coupled third-order system. Decoupling needs to be considered in controller design. LADRC has the ability to estimate the external disturbance and internal disturbance and transform the system into an ideal system through state feedback [32].

3. LADRC Controller Design

3.1. Structure of the LADRC Controller

According to the LCL system model, the *d*-axis and *q*-axis in the *d-q* coordinate system are dual. The *d*-axis analysis is taken as an example. According to the standard ADRC proposed by Han, the structure of LADRC controller with model information is shown as Figure 3. The known information f'_{0d} and f'_{0q} can be obtained from Formula (7).
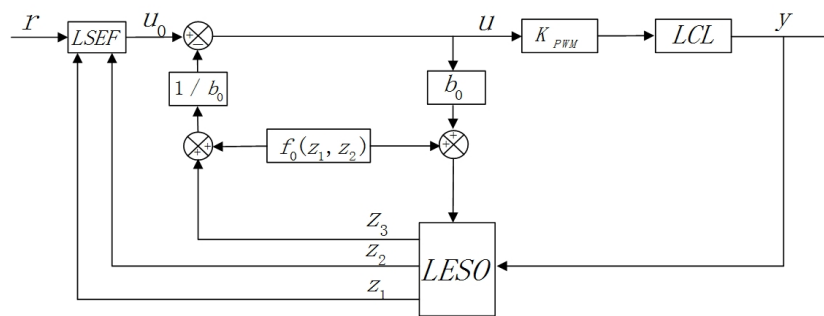

Figure 3. Linear active disturbance rejection control (LADRC) controller with model information.

3.2. LESO Design

According to the state equation, state variables are redefined ($i'_{2d} = z_{1d}, \frac{di'_{2d}}{dt} = z_{2d}, f'_d = z_{3d}$) and extended state variables f'_d are added to rewrite Formula (6), the model is expressed as Formula (8).

$$
\begin{cases}
\dot{z}_d = \mathbf{A_d} z_d + \mathbf{B_d} u_{id} + \mathbf{E_d} \dot{f}'_d, \\[2mm]
y_d = \mathbf{C_d} z_d.
\end{cases}
\tag{8}
$$

The matrix is represented as Formula (9).

$$
\mathbf{z_d} = \begin{pmatrix} z_{1d} & z_{2d} & z_{3d} \end{pmatrix}^T, \mathbf{A_d} = \begin{pmatrix} 0 & 1 & 0 \\ -\frac{1}{L_2C} & 0 & 1 \\ 0 & 0 & 0 \end{pmatrix}, \mathbf{B_d} = \begin{pmatrix} 0 & b_0 & 0 \end{pmatrix}^T,
$$

$$
\mathbf{C_d} = \begin{pmatrix} 1 & 0 & 0 \end{pmatrix}, \mathbf{E_d} = \begin{pmatrix} 0 & 0 & 1 \end{pmatrix}. \tag{9}
$$

Based on Formula (8), the state equation of LESO is constructed as Formula (10).

$$
\frac{d\hat{z}_d}{dt} = \mathbf{A_d}\hat{z}_d + \mathbf{B_d}u_{id} + L_d(y_d - \mathbf{C_d}\hat{z}_d). \tag{10}
$$

where, L_d is the observer gain vector and recorded as: $L_d = \begin{pmatrix} \beta_1 & \beta_2 & \beta_3 \end{pmatrix}^T$, $\hat{z}_d$ is the state vector of the extended state observer.

Subtracting Formula (8) from Formula (10), the error formula can be obtained as Formula (11).

$$
\frac{de_d}{dt} = (\mathbf{A_d} - L_d\mathbf{C_d})e_d + \mathbf{E_d}\dot{f}'_d. \tag{11}
$$

where $e_d = z_d - \hat{z}_d$,

$$
\mathbf{A_d} - L_d\mathbf{C_d} = \begin{pmatrix} -\beta_1 & 1 & 0 \\ -\beta_2 - \frac{1}{L_2C} & 0 & 1 \\ -\beta_3 & 0 & 0 \end{pmatrix}. \tag{12}
$$

In order to guarantee the stability of the LESO, the poles of the LESO are placed in the left half plane. As we design the observer poles are all located at $-\omega_o$, the state observer will be inherently stable and parameters are selected as Formula (13).

$$
\begin{aligned}
\lambda(s) &= (s + \omega_o)^3 = s^3 + 3\omega_o s^2 + 3\omega_o^2 s + \omega_o^3 \\
&= s^3 + \beta_1 s^2 + (\beta_2 + \frac{1}{L_2C})s + \beta_3.
\end{aligned} \tag{13}
$$

The gain of the observer can be written as Formula (14).

$$
\begin{cases} \beta_1 = 3\omega_o, \\ \beta_2 = 3\omega_o^2 - \dfrac{1}{L_2C}, \\ \beta_3 = \omega_o^3. \end{cases} \tag{14}
$$

In this paper, part of the disturbance information is added to the controller through modeling. When disturbance information is known, adding part of the signal to the controller can reduce the bandwidth and noise sensitivity of LADRC controller without substantially affecting the control accuracy [33].

3.3. Controller Design

The process of trasforming a physical modeling system into an integral series system is called dynamic compensation linearization. The effect is similar to the integral part of the PID, but it avoids the negative impact of the integral link. Take the system control law as Formula (15).

$$
\begin{cases} u_0 = k_p(r - \hat{z}_1) - k_d\hat{z}_2, \\ u = \dfrac{u_0 - f_0(\hat{z}_1, \hat{z}_2) - \hat{z}_3}{b_0}. \end{cases} \tag{15}
$$

where u_0 is the output of the error feedback law, r is the given reference value, k_p and k_d, which are the gains of PD control law. And $\hat{z}_1$, $\hat{z}_2$, and $\hat{z}_3$ are observations of z_1, z_2, and z_3.

The transfer function of the reference value r to the output y is shown as Formula (16).

$$G_{c1} = \frac{k_p}{s^2 + k_d s + k_p}. \tag{16}$$

To configure the closed-loop pole at $-\omega_c$, there is the following formula:

$$\begin{aligned} (s + \omega_c)^2 &= s^2 + 2\omega_c s + \omega_c^2 \\ &= s^2 + k_d s + k_p. \end{aligned} \tag{17}$$

According to Formula (17), the gain of the PD control law can be written as follows:

$$\begin{cases} k_p = \omega_c^2, \\ k_d = 2\omega_c. \end{cases} \tag{18}$$

In general, the relationship between ω_o and ω_c is $\omega_o = 3 \sim 10\omega_c$ [10], in this paper, however, it is $\omega_o = 6\omega_c$. If the control effect needs to be further optimized, the influence of each parameter in [34] on the decoupling and stability of the system can be obtained. This paper only gives a conclusion:

1. Calculate b_0 according to $b_0 = \dfrac{R_d}{L_1 L_2}$.
2. Determine the relationship between ESO bandwidth and controller bandwidth, generally take $\omega_o = 3 \sim 10\omega_c$, but not absolute, and can be adjusted according to the actual system.
3. Increase ω_c until the system noise amplification causes the system to be unstable, and then appropriately reduce w_c, taking into account the dynamic characteristics and stability of the system.
4. Appropriately increase β_3 until the closed-loop dynamic performance of the system reaches the desired index, appropriately reduce β_2, and enhance the LADRC disturbance rejection ability.
5. Appropriately reduce b_0 until the disturbance rejection ability is best.

4. Frequency Domain Analysis

LADRC can be equivalent to the series structure of PID and a low-pass filter. In the high-frequency part, the gain of LADRC controller to high-frequency resonance current is smaller because of the attenuation characteristics of the low-pass filter so that the resonance peak can be suppressed. Compared with PID, LADRC has better suppression performance for the resonance of the LCL filter. For the sake of generality, this paper takes a standard second-order as an example, and the system model is as follows [35]:

$$\begin{cases} \dot{x}_1 = x_2, \\ \dot{x}_2 = x_3 + b_0 u, \\ \dot{x}_3 = \dot{f}, \\ y = x_1. \end{cases} \tag{19}$$

The state equation of LESO can be written as follows:

$$\begin{cases} \dot{\hat{z}}_1 = \beta_1(y - \hat{z}_1) + \hat{z}_2, \\ \dot{\hat{z}}_2 = \beta_2(y - \hat{z}_1) + \hat{z}_3 + b_0 u, \\ \dot{\hat{z}}_3 = \beta_3(y - \hat{z}_1). \end{cases} \tag{20}$$

and the controller is as follows:

$$u = \frac{k_p(r - \hat{z}_1) - k_d \hat{z}_2 - \hat{z}_3}{b_0}. \tag{21}$$

Substituting Formula (21) into Formula (20), the formula can be as follows:

$$\begin{cases} \dot{\hat{z}}_1 = -\beta_1\hat{z}_1 + \hat{z}_2 + \beta_1 y, \\ \dot{\hat{z}}_2 = -(\beta_2 + k_p)\hat{z}_1 - k_d\hat{z}_2 + \beta_2 y + k_p r, \\ \dot{\hat{z}}_3 = -\beta_3\hat{z}_1 + \beta_2 y. \end{cases} \quad (22)$$

Formula (22) is subjected to Laplace transform, and the solved $\hat{z}_1, \hat{z}_2, \hat{z}_3$ are brought into Formula (21) to obtain Formula (23). The system is regarded as a subsystem with two inputs and one output, where the inputs are r and y and the outputs are u. The block diagram is shown in Figure 4.

$$\begin{aligned} U(s) = & -\frac{1}{s}\frac{(\beta_1 k_p + \beta_2 k_d + \beta_3)s^2 + (\beta_2 k_p + \beta_3 k_d)s + \beta_3 k_p}{b_0[s^2 + (\beta_1 + k_d)s + \beta_1 k_d + \beta_2 + k_p]}Y(s) \\ & + \frac{k_p(s^3 + \beta_1 s^2 + \beta_2 s + \beta_3)}{b_0 s[s^2 + (\beta_1 + k_d)s + \beta_1 k_d + \beta_2 + k_p]}R(s), \\ = & -C(s)Y(s) + C(s)H(s)R(s). \end{aligned} \quad (23)$$

where,

$$\begin{aligned} C(s) &= \frac{1}{s}\frac{(\beta_1 k_p + \beta_2 k_d + \beta_3)s^2 + (\beta_2 k_p + \beta_3 k_d)s + \beta_3 k_p}{b_0[s^2 + (\beta_1 + k_d)s + \beta_1 k_d + \beta_2 + k_p]}, \\ H(s) &= \frac{k_p(s^3 + \beta_1 s^2 + \beta_2 s + \beta_3)}{(\beta_1 k_p + \beta_2 k_d + \beta_3)s^2 + (\beta_2 k_p + \beta_3 k_d)s + \beta_3 k_p}. \end{aligned} \quad (24)$$
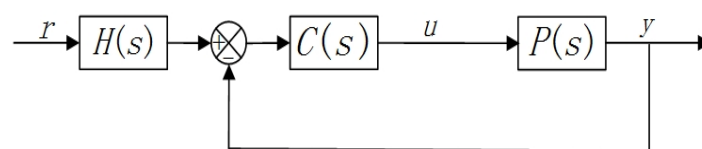

Figure 4. The transformation function block diagram of LADRC.

According to the parameterization of the bandwidth, the available parameters are as follows:

$$\begin{aligned} & b_0 \approx \frac{R}{L_1 L_2}, \omega_o = 3\omega_c, k_p = 2\omega_c, k_d = \omega_c^2, \\ & \beta_1 = 3\omega_o, \beta_2 = 3\omega_o^2, \beta_3 = \omega_o^3. \end{aligned} \quad (25)$$

According to Formula (24), rewrite $C(s)$ as follows:

$$\begin{aligned} C(s) = & \frac{(\beta_1 k_p + \beta_2 k_d + \beta_3)s^2 + (\beta_2 k_p + \beta_3 k_d)s + \beta_3 k_p}{b_0(\beta_1 k_d + \beta_2 + k_p)s} \cdot \frac{\beta_1 k_d + \beta_2 + k_p}{s^2 + (\beta_1 + k_d)s + \beta_1 k_d + \beta_2 + k_p} \\ = & (K_D s + K_P + K_I\frac{1}{s})\frac{\omega_n^2}{s^2 + 2\xi\omega_n s + \omega_n^2} \\ = & C_{PID}(s)F_L(s). \end{aligned} \quad (26)$$

where,

$$K_P = \frac{\beta_2 k_p + \beta_3 k_d}{b_0(\beta_1 k_d + \beta_2 + k_p)}, K_I = \frac{\beta_3 k_p}{b_0(\beta_1 k_d + \beta_2 + k_p)}, K_D = \frac{\beta_1 k_p + \beta_2 k_d + \beta_3}{b_0(\beta_1 k_d + \beta_2 + k_p)}. \quad (27)$$

and

$$\omega_n = \sqrt{\beta_1 k_d + \beta_2 + k_p}, \xi = \frac{\beta_1 + k_d}{2\sqrt{\beta_1 k_d + \beta_2 + k_p}}. \quad (28)$$

In the Formulas (26) and (27) above, k_p and k_d represent the PD gain in LADRC, while K_P, K_I, and K_D represent the proportional, integral, and differential gain in PID. The Bode diagram of the low-pass filter $F_L(s)$ is as shown in Figure 5a. The Bode plots of *PID*, *LADRC*, and *PI* for different ω_o values are shown in Figure 5b–d.

According to Figure 5a, the Bode diagram of F_L exhibits the characteristics of a second-order low-pass filter. According to Figure 5b–d, in the process of wide-scale change, the direction of the bode diagram between LADRC, PI, and PID is basically unchanged. Among them, the controller of PID increases with the increase of frequency, which is extremely unfavorable for high-frequency signals. Compared with LADRC, the PI controller is equal in the low-frequency band, while the gain of LADRC is higher in the intermediate frequency band, so the response speed of LADRC is faster, and in the high-frequency band, the attenuation of LADRC is more than that of the PI controller. The attenuation characteristics of the low-pass filter in LADRC at high-frequencies make controller have better high-frequency rejection than PI.
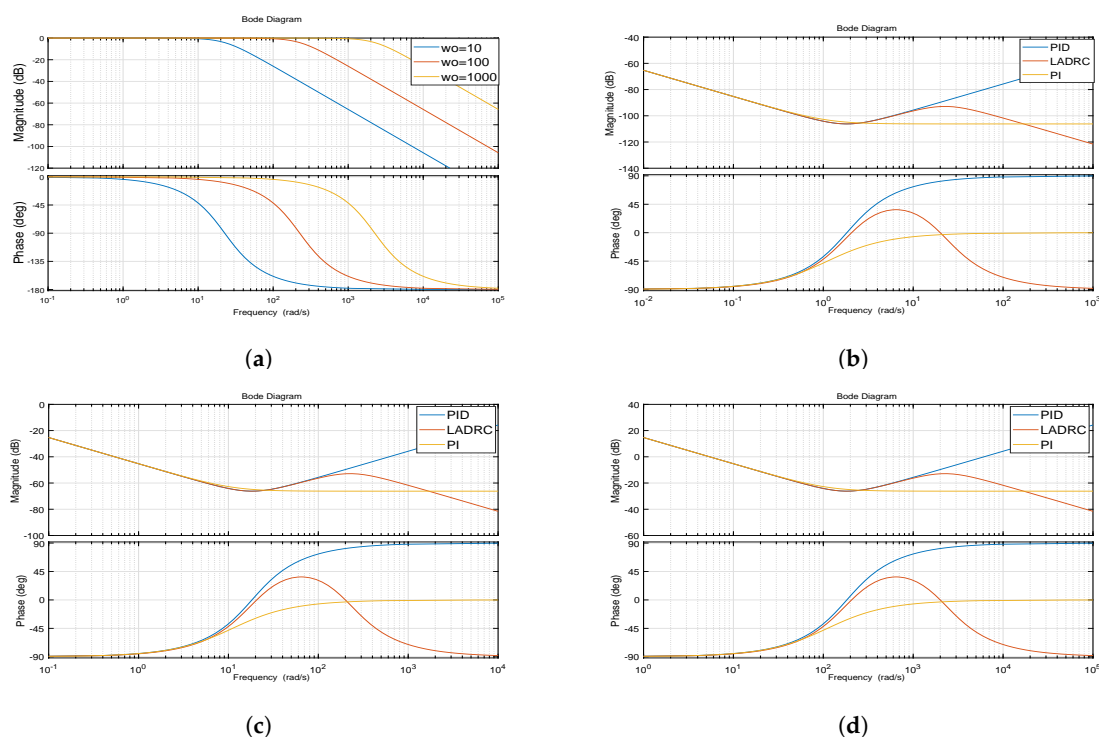

(a)

(b)

(c)

(d)

Figure 5. (**a**): Bode diagram of $F_L(s)$; (**b**): Bode diagram of *LADRC*, *PID* and *PI* under $\omega_o = 10$; (**c**): Bode diagram of *LADRC*, *PID* and *PI* under $\omega_o = 100$; (**d**): Bode diagram of *LADRC*, *PID* and *PI* under $\omega_o = 1000$.

For the different characteristics of the controller, draw the open-loop Bode diagram of the LCL filter in series with different controller in Figure 6a. The parameters of the LCL-type filter and passive damping resistance are shown as below:

$$L_1 = 0.2 \text{ mH}, L_2 = 0.042 \text{ mH}, C = 30 \text{ μF}, R_d = 0.5 \text{ Ω}.$$

According to Figure 6a, a resonance peak appears, which causes the harmonics around the resonant frequency in the circuit to amplify into the system. After adding PID, PI, and LADRC, the resonance phenomenon is partially suppressed. The PID controller is unable to deal with high-frequency signal, and the suppression effect of PI in the middle frequency band is better than that of LADRC. LADRC is better than PI in the high-frequency range.

Figure 6b shows the open-loop Bode diagram of the LCL filter with passive damping resistance in series with a different controller. According to Figure 6b after the series resistance is applied to the LCL

circuit, the resonance peak disappears. However, there is still a partial rise around the resonance peak. The PI and LADRC controllers have a substantially coincident gain of less than 1000 rad/s, and the LADRC effect is not as good as PI at the intermediate frequency range. LADRC is more effective at attenuating signals at higher frequencies than PI. If the pole position of the LADRC is adjusted, the frequency characteristics of the LADRC can be changed to enhance the LADRC harmonic suppression capability, especially near the switching frequency.
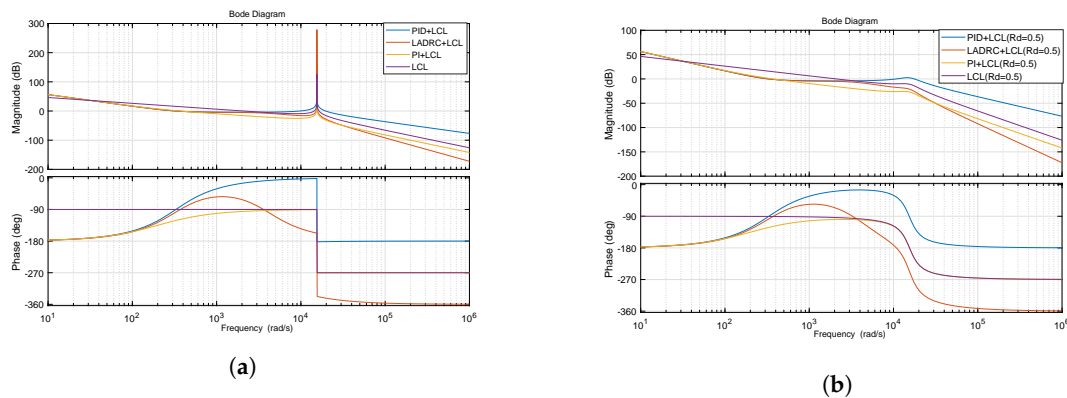
Figure 6. (**a**): Bode diagram of LCL in series with different controllers; (**b**): Bode diagram of LCL with passive damping resistance in series with different controllers.

By reducing β_2, increasing β_3, redrawing the Bode diagram of LADRC and adjusting the gain of LADRC in each frequency band, the LADRC harmonic suppression capability is improved. The new changed observer gains are as follows:

$$\begin{cases} \beta_1 = 3\omega_o, \\ \beta_2 = 0.05\omega_o^2, \\ \beta_3 = 3\omega_o^3. \end{cases} \tag{29}$$

Other parameters are still calculated according to Formulas (27) and (28). Then repeating those steps will get Figure 7a,b.
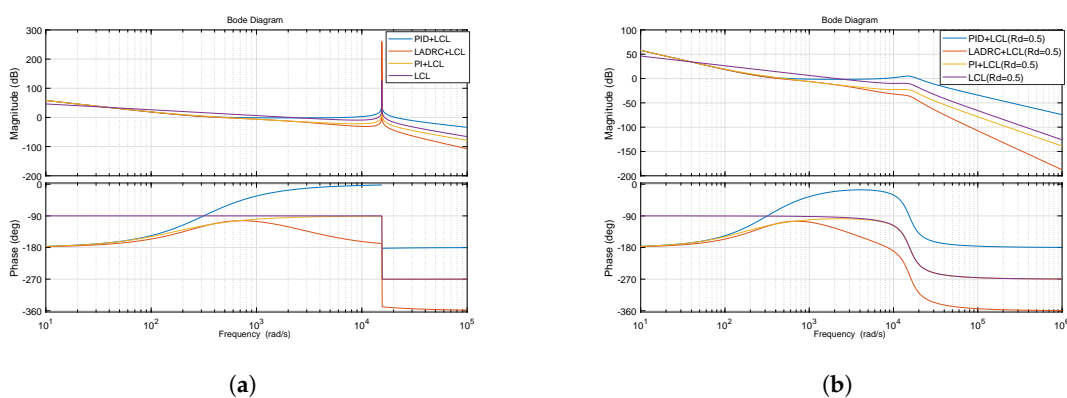

Figure 7. (**a**): Bode diagram of LCL in series with different controllers; (**b**): Bode diagram of LCL with passive damping resistance in series with different controllers.

According to Figure 7a,b, the gain margin and phase margin corresponding to the two different parameters selection schemes are listed in Table 1.

Comparing two different parameter-selected methods, LADRC is better than PI in both the resonance suppression capability and the dynamic performance of the system under the condition of the novel method selection parameters. Although reducing β_2 and increasing β_3 are beneficial to

resonance suppression and quicken the dynamic response speed effectively, the stability of the system is degraded. In the practical application, it needs to weigh the advantages and disadvantages.

Table 1. Phase margin and gain margin of PI and LADRC.

Parameters	$\beta_1 = 3\omega_o$ $\beta_3 = \omega_o^3$	$\beta_2 = 3\omega_o^2$	$\beta_1 = 3\omega_o$ $\beta_3 = 3\omega_o^3$	$\beta_2 = 0.05\omega_o^2$
	Gain margin	Phase margin	Gain margin	Phase margin
PI	37 dB	49.7°	23.5 dB	70.9°
LADRC	30.6 dB	55.4°	30.3 dB	69.4°

According to Table 1, the improved method is used to design the observer gain so that the LADRC has an amplitude margin greater than the amplitude margin of the PI, and the phase margin is substantially equal. This demonstrates that LADRC has better dynamic characteristics and robustness under new parameters selection.

5. Active Power Filter Design

In this section, harmonic current detection is based on the *ip-iq* method of instantaneous reactive power, which uses the TD filter instead of the Butterworth filter, which improves compensation and response of APF.

5.1. The Improved Harmonic Detection Algorithm

The instantaneous space vector method based on instantaneous reactive power theory is currently the most widely used detection method. When the method only detects the reactive current, the detection result can be obtained without delay. When the harmonic current is detected, there will be different delays due to the difference in the harmonics of the current to be detected and the filter used, but the delay may not exceed one cycle at most. For the three-bridge rectifier circuit, the most typical harmonic source in the power system, the detection delay is about 1/6 of a cycle.

The traditional APF detects the load current, the harmonics are obtained by the harmonic detection algorithm, and a opposite harmonic is generated by the inverter so that the load current contains only the fundamental component. However, such a detection algorithm is an open-loop algorithm. At the same time, the load harmonics and the grid harmonics are detected, and the harmonic command current is simultaneously sent to the inverter so that the grid current detection path makes the system form a closed-loop system. The algorithm block diagram is shown in Figure 1. The transformation matrices are as seen in Formula (30).

$$\mathbf{C_{32}} = \frac{2}{3}\begin{pmatrix} 1 & -\frac{1}{2} & -\frac{1}{2} \\ 0 & -\frac{\sqrt{3}}{2} & \frac{\sqrt{3}}{2} \end{pmatrix}, \mathbf{C} = \begin{pmatrix} \sin(\omega_g t) & -\cos(\omega_g t) \\ -\cos(\omega_g t) & -\sin(\omega_g t) \end{pmatrix}, \mathbf{C_{23}} = \begin{pmatrix} 1 & 0 \\ -\frac{1}{2} & \frac{\sqrt{3}}{2} \\ -\frac{1}{2} & -\frac{\sqrt{3}}{2} \end{pmatrix}. \quad (30)$$

The TD algorithm is as follows:

$$\begin{cases} fh = fhan(x_1(k) - v(t), x_2(k), r, h_0), \\ x_1(k+1) = x_1(k) + hx_2(k), \\ x_2(k+1) = x_2(k) + hfh, \\ y(k+1) = x_1(k+1). \end{cases} \quad (31)$$

where h is the discretization step size and function $fhan$ is defined as follows:

$$
\begin{cases}
d = rh_0^2, \\
a_0 = h_0 x_2, \\
y = x_1 + a_0, \\
a_1 = \sqrt{d(d + 8\,|y|)}, \\
a_2 = a_0 + sign(y)(a_1 - d)/2, \\
a = (a_0 + y)fsg(y, d) + a_2(1 - fsg(y, d)), \\
fsg(x, d) = (sign(x + d) - sign(x - d))/2, \\
fhan = -r\left(\dfrac{a}{d}\right)fsg(a, d) - rsign(a)(1 - fsg(a, d)),
\end{cases}
\tag{32}
$$

where, r is the speed factor of the TD tracking signal. The larger r is, the faster the TD tracks the target signal. h_0 is the filtering factor. The larger the h_0, the better the TD filtering effect, but the slower the response speed.

5.2. Low-Pass Filter Design

The traditional *ip-iq* harmonic detection algorithm uses a Butterworth filter to filter out AC component. Although the Butterworth filter has better filtering effects, it will have a large overshoot. Not only that, if the order of the filter is increased, the response speed will be significantly reduced. In this paper, we propose to use a nonlinear TD instead of a low-pass filter to solve the contradiction between the response speed of the Butterworth filter and the filtering effect, so that the filtering is fast and no overshoot. The frequency characteristic curve of TD is shown in Figure 8.

According to Figure 8, it can be seen that the nonlinear characteristic of the nonlinear TD is reflected in the fact that the difference in amplitude of the input signal also causes a difference in frequency characteristics and not only in relation to the frequency of the input signal. The amplitude-frequency characteristic curve of TD is obviously a fold line composed of two straight lines, and the phase-frequency curve is near the corner frequency, and the phase shift is quickly reduced to $-180°$, which is an ideal phase-frequency characteristic.
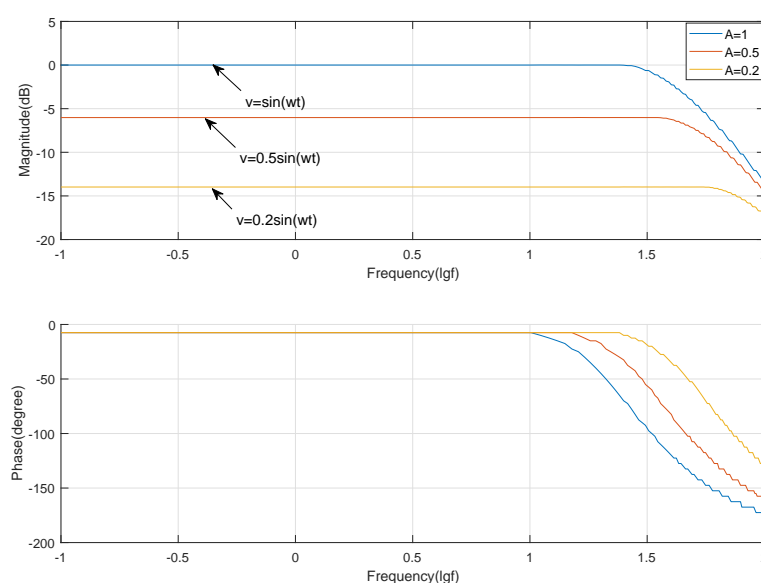

Figure 8. Bode diagram of the tracking differentiator (TD).

In addition to the *r* determining the bandwidth of the TD, the filtering factor h_0 also determines the bandwidth and gain. Choosing the appropriate h_0 can improve the frequency characteristics of the TD. If h_0 increases, the gain can be reduced while the bandwidth increases. Because TD is used as a low-pass filter in APF, increasing h_0 can make the AC component sufficiently attenuate. While DC component is not affected, it can reduce the overshoot of the system to achieve fast no-overshoot filtering.

Butterworth low-pass filter has a large overshoot in the filtering process. TD has *fhan* function, thus avoiding the overshoot of the filter and solving the problem between fastness and overshoot. The *fhan* function can reach the setpoint in a finite step and stay there, and *fhan* softens the input signal or arranges the transition process so that the system quickly keeps the given signal without overshoot.

6. Simulation Results

In this section, the performance of the designed microgrid with the proposed strategy is evaluated through the simulation results, which are conducted through MATLAB/SIMULINK under three situations. For convenience of description, Scheme I is the method proposed strategy, and Scheme II is a conventional method. The detailed configuration scheme of each scheme is shown in Table 2. The parameters of the grid, grid-connected inverter, and APF are shown in Table 3. The grid inductance is to filter out the harmonics near the switching frequency generated by the two inverters. The parameters of controllers are shown in Table 4.

Table 2. Control strategy for different scheme.

Scheme	I	II
Grid-connected inverter	LADRC	PI
APF	PI	PI

Table 3. Circuit parameters.

Symbol	Description	Value
g_{abc}	Grid phase voltage	220 V
L_g	Inductance of grid	3 mH
L	Inductance of nonlinear load	9 mH
R	Resistance of nonlinear load	10 Ω
f_s	Switching frequency of grid-connected inverter	10 kHz
f_c	Switching frequency of APF	20 kHz
L_1	Filter-side inductance	0.2 mH
C	Filter-side capacitance	30 μF
L_2	Grid-side inductance	0.042 mH
R_d	Passive damping resistance	0.5 Ω
V_{dc1}	DC voltage source of grid-connected inverter	1000 V
V_{dc2}	DC voltage source of APF	1400 V
L_3	Filter inductance of APF	8.6 mH

Table 4. Controller parameters.

	Scheme I			Scheme II	
Symbol	Value	Symbol	Value	Symbol	Value
ω_c	600 rad/s	k_{p1}	3.6×10^5	k_p	2
ω_o	3600 rad/s	k_{d1}	1.2×10^3	k_i	200
b_0	9.5×10^8	K_p	7	K_p	7
β_1	1.08×10^4	K_i	60	K_i	60
β_2	6.48×10^5	i_{pccd}	80 A	i_{pccd}	80 A
β_3	1.4×10^{11}	i_{pccq}	0 A	i_{pccq}	0 A

In Table [4], k_{p1} and k_{d1} represent the proportional differential control gain in the LADRC controller for the grid-connected inverter, K_p and K_i represent the proportional-integral control gain of the PI controller in the APF, and k_p and k_i represent parameters of the PI controller of the grid-connected inverter. The parameters of LADRC controller are set according to Formula (14), and then according to the system performance requirements, reduce β_2 and increase β_3 appropriately until the system performance meets the requirements.

6.1. Case I

This case is that the nonlinear load is connected to the grid, and the grid-connected inverter and APF are sequentially connected. The objective of the simulation is to validate the harmonics reduction performance of the proposed strategy. In order to verify that LADRC has better dynamic characteristics than PI, the simulation compares the grid-connected current control effect and harmonic suppression effect.

In this simulation experiment, the nonlinear load is a three-phase uncontrolled rectifier circuit. The simulation runs for a total of 0.3 s, and the grid-connected inverter is connected at 0.02 s, and the APF is accessed at 0.1 s. Figure [9] shows the FFT analysis results of the nonlinear load current and the grid current when the system is connected to the power equipment at different times and the grid current after the cut-in time.
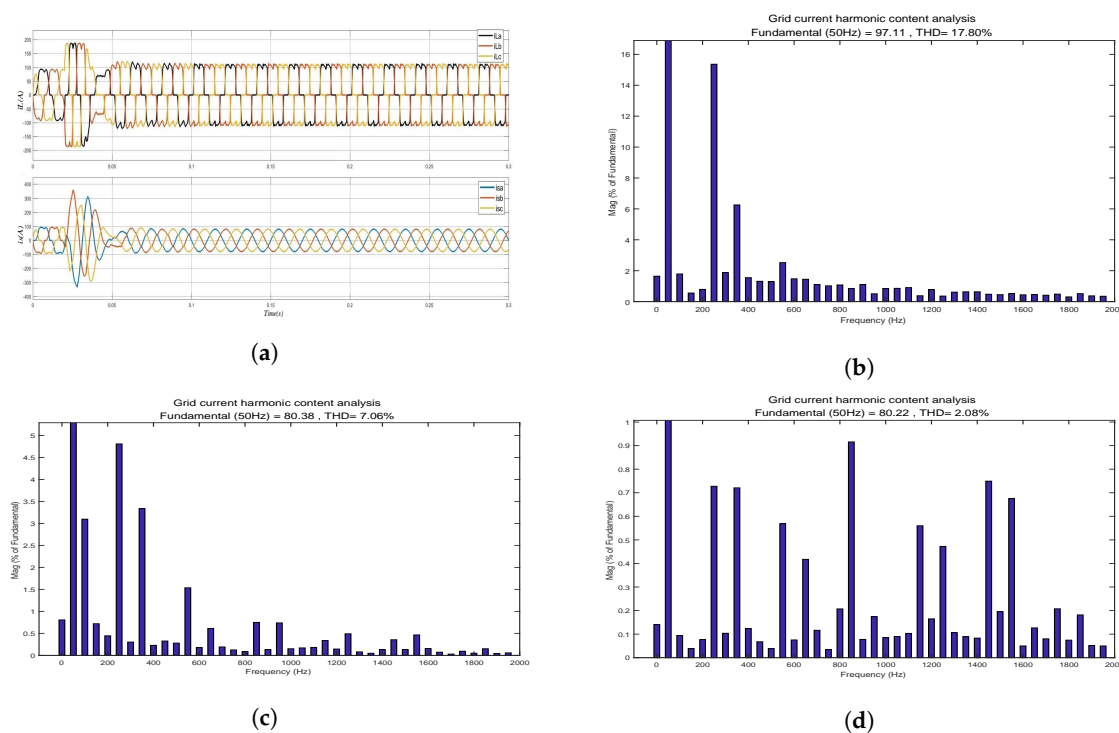

(**a**)

(**b**)

(**c**)

(**d**)

Figure 9. Scheme I: (**a**) nonlinear load current and grid current; (**b**) the FFT result of the nonlinear load current at the 0 s; (**c**) the FFT result of the grid current at the 0.07 s; (**d**) the FFT result of the grid current at the 0.15 s.

By comparing Figures [9]a and [10]b, LADRC is stable in two cycles, while the PI controller requires three and a half cycles to stabilize. According to Figures [9]b and [10]b, the harmonic content of the system is 17.8% when the nonlinear load is connected to the system. As can be seen from comparing Figures [9]c and [10]c, the harmonic content is 7.06% and 6.02% at 0.07 s seconds under different controller. At this time, the grid current is bigger than the given value, and the magnitude of the harmonic current is constant, resulting in a lower harmonic content than using LADRC. By comparing Figures [9]d and [10]d, after the APF is connected to the system, the system harmonics are 2.08% and 5.39%. From the results, LADRC has better dynamic performance and harmonic suppression. The former can reduce the THD

(Total Harmonic Distortion) of the distortion current to 2.1%, while the latter can only reduce the current distortion rate to 5.39%, which can not satisfies the IEEE Standard. A comparison of the filtering effects of TD and Butterworth in the simulation is shown in Figure 11.

According to Figure 11, it can be seen that TD has a better filtering effect and dynamic characteristics, and avoids overshoot, improving the dynamic characteristics of the whole system. TD stabilized around 0.2 s, and Butterworth stabilized around 0.32 s. TD is approximately 37.5% faster than the Butterworth.

6.2. Case II

This case is when the system is running stably, the reference value is abrupt. In order to verify the disturbance rejection ability and the dynamic performance of the proposed strategy under reference value changing condition, the simulation runs for a total of 0.3 s. At 0.1 s, the *d*-axis reference current signal steps from 80 A to 113 A, and at 0.2 s, the *q*-axis reference signal steps from 0 A to 20 A. Figure 12 and Figure 13 show the response curves of the currents of the Scheme I and the Scheme II at PCC of the reference current abrupt change, respectively.

(**a**)

(**b**)

(**c**)

(**d**)
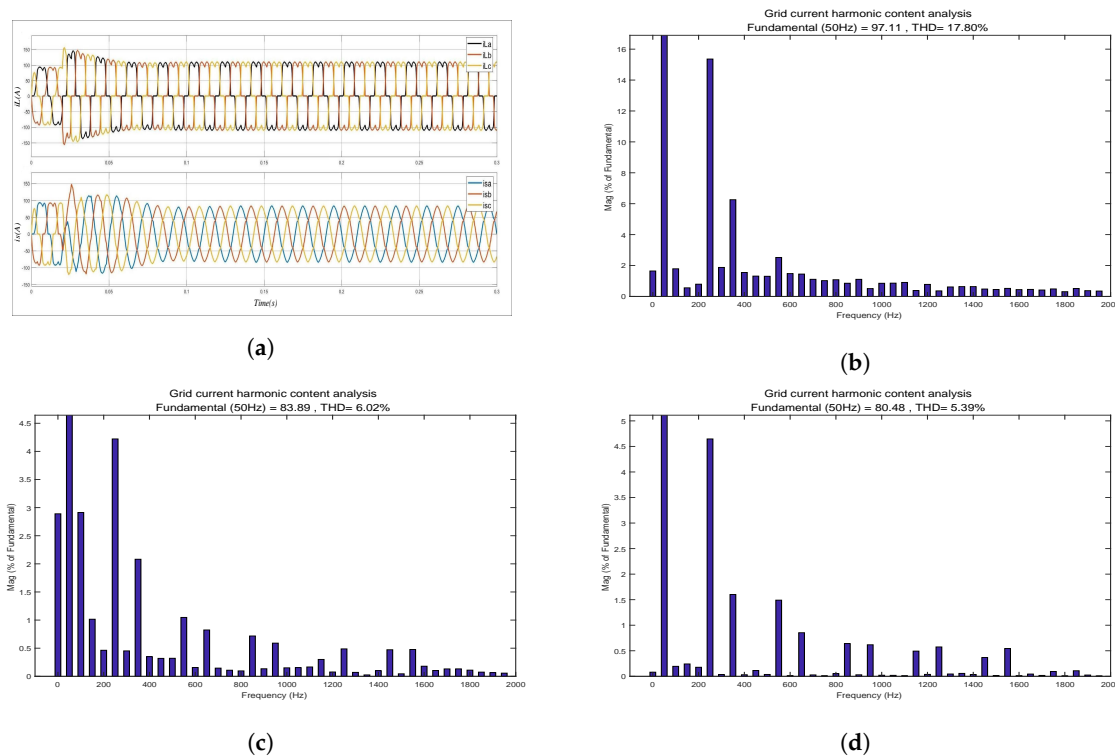
Figure 10. Scheme II: (**a**) nonlinear load current and the grid current; (**b**) the FFT result of the grid current at the 0 s; (**c**) the FFT result of the grid current at the 0.07 s; (**d**) the FFT result of the grid current at the 0.15 s.

By comparing Figures 12 and 13, Scheme I can reach steady-state in a shorter time, and in the case of a sudden change in the *d*-axis reference current, there is only a small effect on the *q*-axis; in the case of a sudden change in the *q*-axis reference current, it basically has no effect on the *d*-axis current. In the case of a sudden change in the reference current, Scheme II not only has a large overshoot of the current but also track the given reference signal for a longer time. The change in the reference signal of either of the *d*-axis and the *q*-axis has a large effect on the current of the other axis. In the case of sudden changes in operating conditions, Scheme I has better disturbance rejection ability and dynamic response than Scheme II.
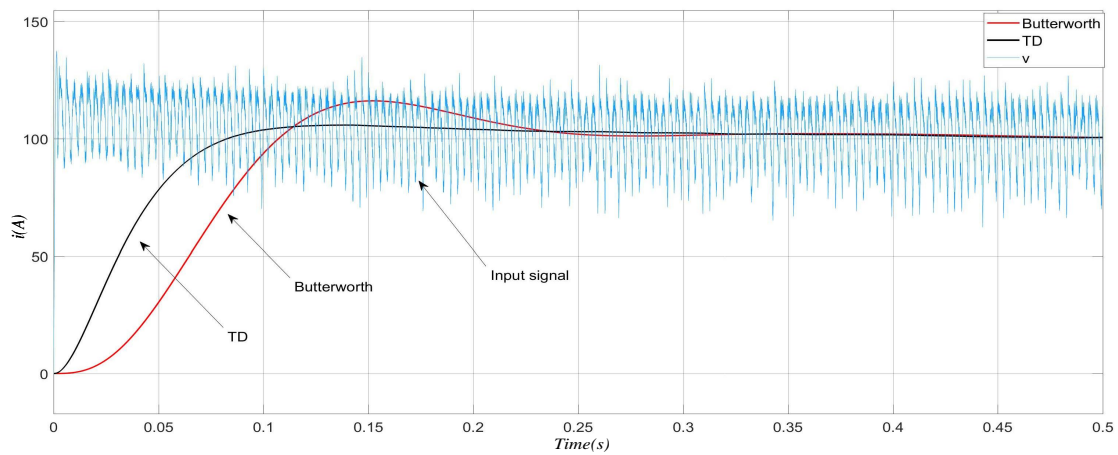
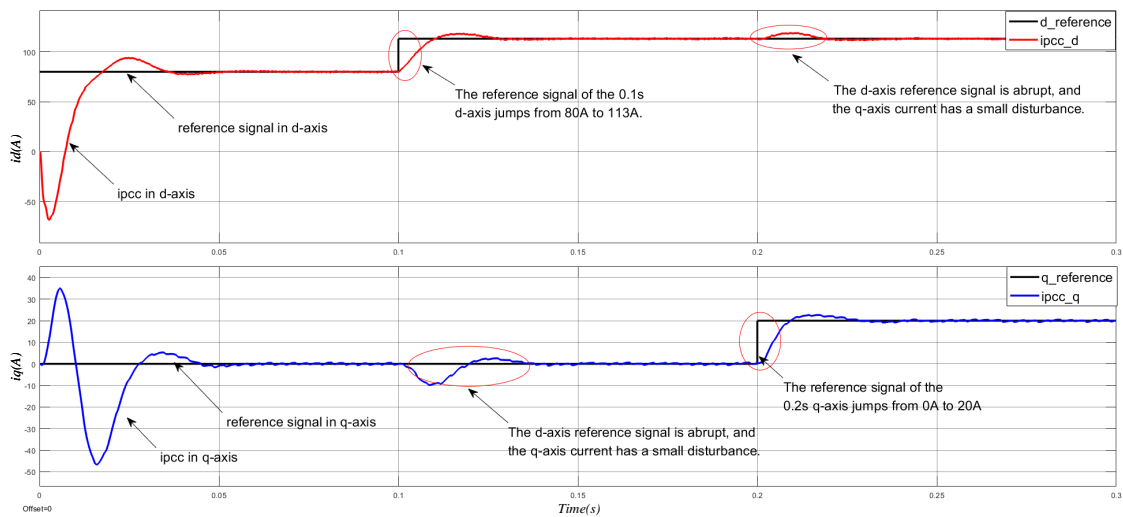**Figure 11.** The response curves of TD and Butterworth.

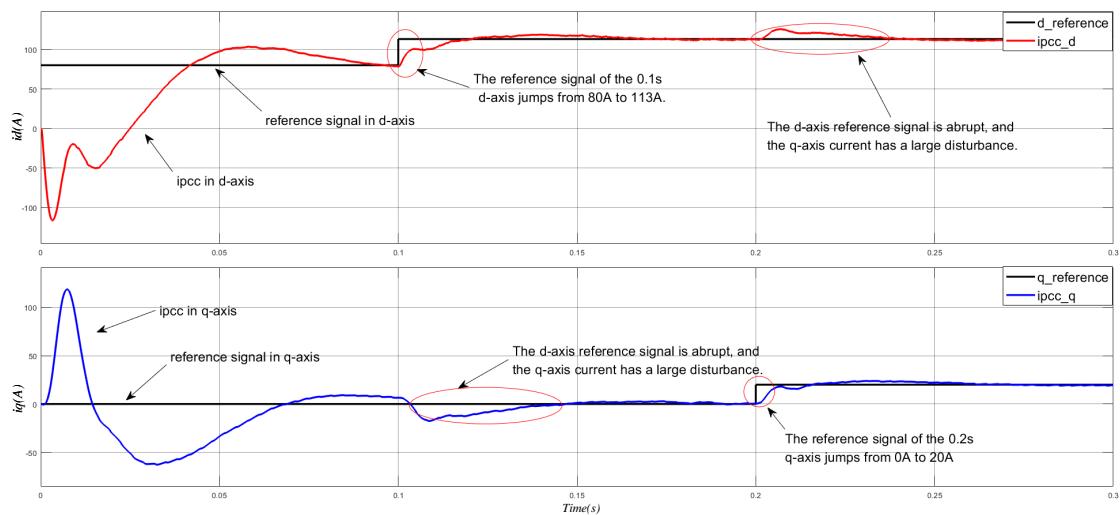**Figure 12.** The point of common coupling current response curve of Scheme I.

Figure 13. The point of common coupling current response curve of Scheme II.

6.3. Case III

This case is that the grid voltage fluctuates repeatedly. When the grid voltage repeatedly fluctuates, the dynamic performance of Scheme I and Scheme II is compared. The simulation runs for a total of 0.3 s. At 0.1 s, the grid voltage drops to 0.6 times the rated voltage. At 0.15 s, the grid voltage recovers the rated voltage. Figure 14 shows the nonlinear load current and the grid current for Schemes I and II in the case of grid voltage fluctuations.

By comparing Figure 14a,b, in the moment of grid voltage drop, Scheme I only needs one and a half cycles to realize the control of grid-connected current, while Scheme II requires two and a half cycle to realize control of grid current. In engineering applications, if the working conditions change rapidly, Scheme I performs better than Scheme II.
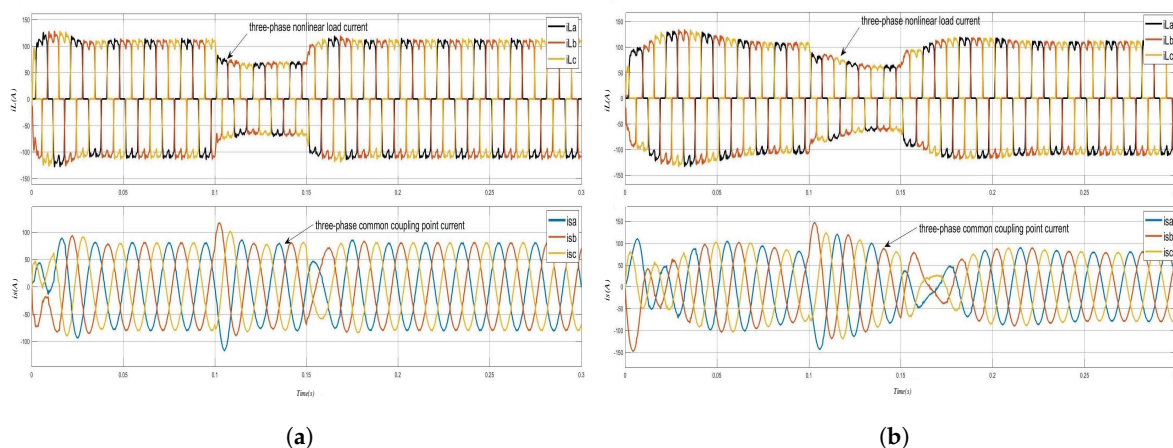

(**a**)   (**b**)

Figure 14. (**a**) Three-phase nonlinear load current and grid current of Scheme I; (**b**) three-phase nonlinear load current and grid current of Scheme II.

According to the above three cases, the disturbance rejection ability and the dynamic response performance of the system, Scheme I is superior to Scheme II in each phase index. The cut-in of the equipment, the sudden change of the reference current, and the sudden change of the grid respectively can be regarded as the total disturbance of the system, because the LADRC controller can observe the external disturbance of the system and the uncertainty of the system through ESO as the total disturbance, and transform the system into the ideal system through dynamic feedback linearization. The simulation proves that Scheme I can eliminate the disturbance as mentioned above through the state feedback. However, the PI controller will generate the corresponding control signal after the error occurs, which means that the PI controller is slower than the LADRC controller. The simulation results are also consistent with the above analysis.

7. Experimental Results

Compared with PI control, the main advantages of the LADRC controller is the attenuation of high-frequency signals, and ESO has the effect of disturbance observation, which makes LADRC better for disturbance rejection. In physical hardware experiments, the electrical characteristics of electrical components change with temperature. Besides, the parasitic resistance of electrical components, such as inductance and capacitance, is often unavoidable, which is a challenge for the controller.

In this paper, an LCL-type with passive damping resistance three-phase three-leg inverter and an L-type three-phase three-leg inverter were built. The LCL-type filter with passive damping resistance was controlled by a Speedgoat semi-physical simulator. The L-type inverter was controlled by a TMS320F28335 digital signal processor microcontroller. The topology of the hardware circuit was the same as that of Figure 1, and the hardware circuit parameters are shown as Table 5. The parameters

of controller are shown Table 6. In this section, two experiments are described to verify the performance of the control strategy described above. The experimental platform is shown in Figure 15.
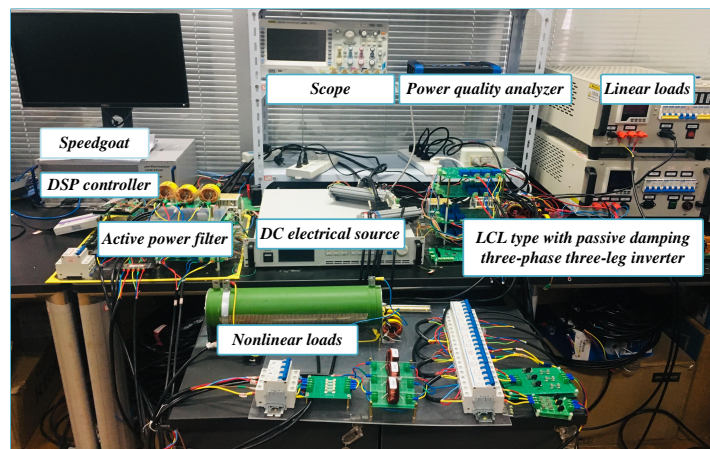

Figure 15. Experimental hardware platform.

Table 5. Experimental circuit parameters.

Symbol	Description	Value
g_{abc}	Grid phase voltage	22 V
L_g	Inductance of grid	3 mH
L	Inductance of nonlinear load	9 mH
R	Resistance of nonlinear load	70 Ω
R_l	Linear load	40 Ω
f_s	Switching frequency of grid-connected inverter	10 kHz
f_c	Switching frequency of APF	20 kHz
L_1	Filter-side inductance	0.2 mH
C	Filter-side capacitance	30 μF
L_2	Grid-side inductance	0.042 mH
R_d	Passive damping resistance	0.5 Ω
V_{dc1}	DC voltage source of grid-connected inverter	140 V
V_{dc2}	DC voltage source of APF	130 V
L_3	Filter inductance of APF	8.6 mH

Table 6. Controller parameters in physical experiment.

	Scheme I			Scheme II	
Symbol	Value	Symbol	Value	Symbol	Value
ω_c	700 rad/s	k_{p1}	4.9×10^5	k_p	25
ω_o	4200 rad/s	k_{d1}	1.4×10^3	k_i	60
b_0	6×10^7	K_p	25	K_p	25
β_1	1.3×10^4	K_i	60	K_i	60
β_2	8.8×10^5	i_{pccd}	1A	i_{pccd}	1A
β_3	2.2×10^{11}	i_{pccq}	0A	i_{pccq}	0A

7.1. Harmonic Suppression Effect without APF

The grid supplies power to the nonlinear and linear loads, after which the grid-connected inverters are connected to the grid. Experimental waveform and THD analysis diagram are shown in Figure 16.

When the grid-connected inverter is not connected, the THD of grid current is 15.25%, which is severely distorted. In order to verify that the grid-connected inverter has partial harmonic suppression effect, the grid-connected reference current is set to 1A, which is slightly smaller than the grid current before the grid-connected inverter is not added. When the grid-connected inverter connected to the grid, the THD drops to 10.31%. The LADRC controller has a second-order low-pass

filter characteristic, which makes it more advantageous when dealing with harmonic currents. However, LADRC has a limited ability to process high-frequency signals. ESO has certain limitations when observing high-frequency disturbance signals. Phase delay and bandwidth problems determine that LADRC can only deal with low-frequency harmonics. Harmonics can also be slightly suppressed by PI controller because the PI controller has high gain in the low-frequency range and low gain in the high-frequency range.
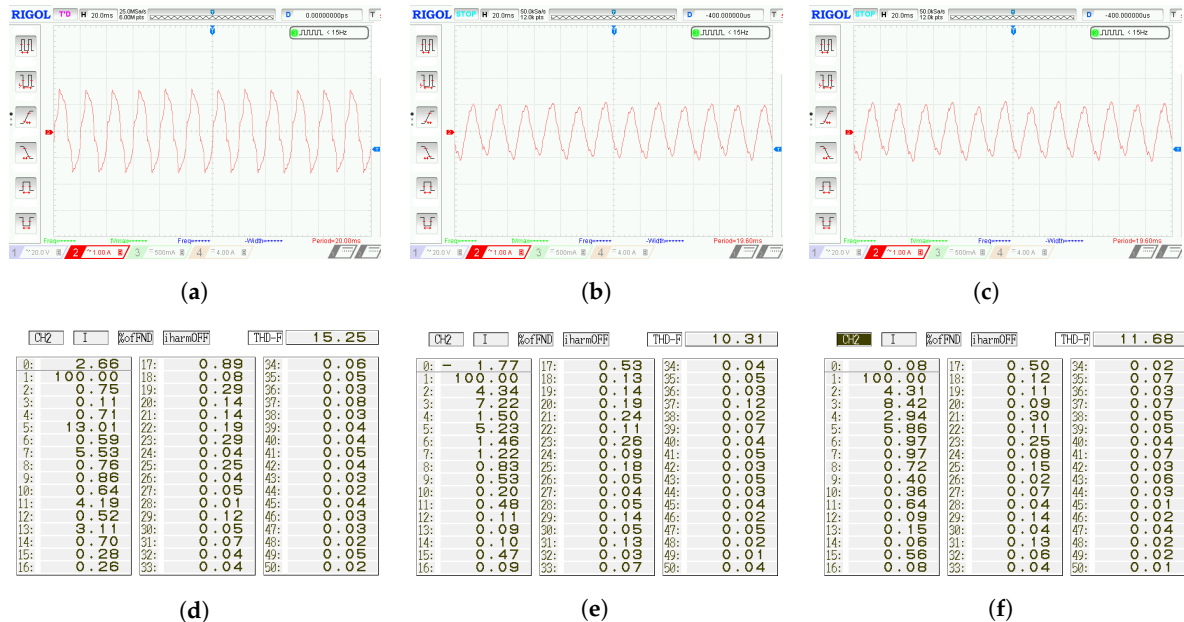

Figure 16. (**a**) Nonlinear load current; (**b**) when the grid-connected inverter is controlled by LADRC the grid current waveform; (**c**) when the grid-connected inverter is controlled by PI, the grid current waveform; (**d**) THD for (**a**); (**e**) THD for (**b**); (**f**) THD for (**c**).

7.2. Harmonic Suppression Effect with APF

Based on Experiment 7.1, during the operation of the grid-connected inverter, access the APF and observe the grid current waveform. Scheme I adopts the LADRC control algorithm for the grid current, and the APF uses the improved *ip-iq* detection method to track the signal. Scheme II control the grid-connected current with PI controller, and the harmonic detection method and harmonic tracking algorithm are consistent with Scheme I.

As can be seen from Figure 17, although the grid-connected inverter can perform harmonic suppression, its effect is limited, and only low-order harmonics can be processed. When APF is connected to the system, the waveform can be significantly improved. Scheme I reduces the harmonic content from 10.31% to 3.18%, while Scheme II reduces it from 11.68% to 5.87%. Scheme I meets international standards and proves that the proposed control strategy is to suppress harmonics while controlling grid-connected current effectively.

8. Discussion

The simulation and experiment results confirm the effectiveness of the proposed control strategy. The composite control strategy can improve the speed and accuracy of the harmonic detection. Due to the existence of the LADRC controller, the system has a strong disturbance rejection ability. By adjusting the different parameters of the ESO, the decoupling ability and dynamic performance of the system can be further improved.

From the experimental results, the grid current still has a harmonic distortion rate of 3.18%. The reason is that the switching frequency of the active power filter is limited, which makes it

impossible for PI controller to track the command harmonics without static error. The track controller can be improved in the next study.

Although the proposed scheme can realize the functions of grid current control and harmonic suppression, its hardware is complex to realize. The system has some difficulty in the debugging process. In the subsequent studies, harmonic detection and compensation method, and grid-connected current control strategy for single inverter can be improved continuously.
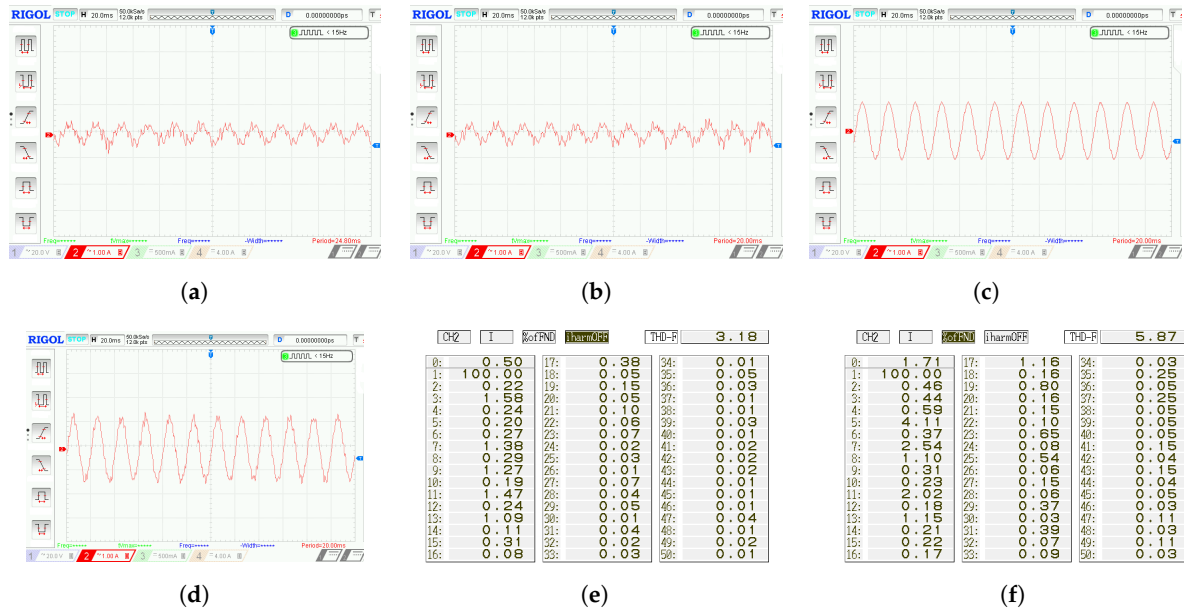

Figure 17. (**a**) The output current of APF of Scheme I; (**b**) the output current of APF of Scheme II; (**c**) the grid current waveform of Scheme I; (**d**) the grid current waveform of Scheme II; (**e**) THD for (**c**); (**f**) THD for (**d**).

9. Conclusions

Conventional active power filters and grid-connected inverters only realize control and compensation of the fundamental or harmonics current. From the perspective of control theory, the system only achieves incomplete control of the current. According to this problem, the author proposes to control the fundamental current through the grid-connected inverter and compensate the harmonics through the active power filter.

LADRC controller with model information is added to the grid-connected inverter to improve dynamic performance and disturbance rejection ability. In the harmonic detection algorithm, TD is used instead of Butterworth filter, which improves the detection speed and accuracy of the algorithm and solves the contradiction between overshoot and rapidity. The novel control strategy proposed by the author achieves the control of the current fundamental wave and the compensation of the harmonics. The author verifies the effectiveness of the proposed strategy through experiments and simulations.

References

1. Ko, S.; Lee, S.; Dehbonei, H.; Nayar, C.V. A Grid-Connected Photovoltaic System with Direct Coupled Power Quality Control. In Proceedings of the 32nd Annual Conference on IEEE Industrial Electronics, IECON 2006, Paris, France, 6–10 November 2006; pp. 5203–5208.
2. Gaafar, M.A.; Shoyama, M. Active Damping for Grid-connected LCL Filter Based on Optimum Controller Design Using Injected Grid Current Feedback Only. In Proceedings of the 2014 IEEE Energy Conversion Congress and Exposition (ECCE), Pittsburgh, PA, USA, 14–18 September 2014; pp. 3628–3633.
3. Rockhill, A.A.; Liserre, M.; Teodorescu, R.; Rodriguez, P. Grid-Filter Design for a Multimegawatt Medium-Voltage Voltage-Source Inverter. *IEEE Trans. Ind. Electron.* **2011**, *58*, 1205–1217. [CrossRef]
4. Benyoucef, A.; Kara, K.; Chouder, A.; Silvestre, S. Prediction-based Deadbeat Control for Grid-connected Inverter with L-filter and LCL-filter. *Electr. Power Components Syst.* **2014**, *42*, 1266–1277. [CrossRef]
5. Mariethoz, S.; Morari, M. Explicit Model-Predictive Control of a PWM Inverter With an LCL Filter. *IEEE Trans. Ind. Electron.* **2009**, *56*, 389–399. [CrossRef]
6. Komurcugil, H.; Altin, N.; Ozdemir, S.; Sefa, I. Lyapunov-Function and Proportional-Resonant Based Control Strategy for Single-Phase Grid-Connected VSI with LCL Filter. *IEEE Trans. Ind. Electron.* **2015**, *63*, 2838–2849. [CrossRef]
7. Shen, G.; Zhu, X.; Zhang, J.; Xu, D. A New Feedback Method for PR Current Control of LCL-Filter-Based Grid-Connected Inverter. *IEEE Trans. Ind. Electron.* **2010**, *57*, 2033–2041. [CrossRef]
8. Zeng, G.; Rasmussen, T.W. Design of Current-controller with PR-regulator for LCL-filter Based Grid-connected Converter. In Proceedings of the IEEE International Symposium on Power Electronics for Distributed Generation Systems, Hefei, China, 16–18 June 2010.
9. Zhang, D.; Chen, Y.; Wu, A.; Zhou, Z. Precision Motion Control of Permanent Magnet Linear Motors. *Int. J. Adv. Manuf. Technol.* **2007**, *35*, 301–308. [CrossRef]
10. Zhao, S.; Tan, K.K. Adaptive Feedforward Compensation of Force Ripples in Linear Motors. *Control. Eng. Pract.* **2005**, *13*, 1081–1092. [CrossRef]
11. Yan, S.; Wang, X.; Chen, H. Decoupling Control of Three-Phase Four-Leg Inverter in Micro-Turbine Power Generation. *Trans. China Electrotech. Soc.* **2012**, *27*, 69–73.
12. Yao, Z.; Xiao, L.; Chen, L. An Improved Decoupling Control Method for Three-phase Grid-connected Inverters with SVPWM. *Autom. Electr. Power Syst.* **2012**, *36*, 99–103.
13. Ning, H.; Xu, D.; Ye, Z.; Zhang, J.; Shen, G.; Zhang, Y.; Jie, M.; Liu, C. Weighted Average Current Control in a Three-Phase Grid Inverter with an LCL Filter. *IEEE Trans. Power Electron.* **2012**, *28*, 2785–2797.
14. Khajehoddin, S.A.; Karimi-Ghartemani, M.; Jain, P.K.; Bakhshai, A. A Control Design Approach for Three-Phase Grid-Connected Renewable Energy Resources. *IEEE Trans. Sustain. Energy* **2011**, *2*, 423–432. [CrossRef]
15. Qu, K.; Ye, T.; Zhao, J. Feedforward Compensation Based Decoupling Control Strategy for Grid-connected Inverter with LCL Filter. *Electr. Drive* **2015**, *45*, 26–30.
16. Qu, K.; Li, W.; Ye, T.; Zhao, J. State Feedback Based Decoupling Control Strategy for Grid-Connected Inverter with LCL Filter. *Trans. China Electrotech. Soc.* **2016**, *31*, 130–138.
17. Han, J. From PID to Active Disturbance Rejection Control. *IEEE Trans. Ind. Electron.* **2009**, *56*, 900–906. [CrossRef]
18. Gao, Z. Scaling and bandwidth-parameterization based controller tuning. In Proceedings of the American Control Conference, Denver, CO, USA, 4–6 June 2003; Volume 6, pp. 4989–4996.
19. Zhu, H.; Wei, G.; Wan-Lu, W.U.; Zhou, C.L. The ADRC Applied in Droop Control Strategy in Microgrid. *Power Syst. Prot. Control.* **2014**, *42*, 61–67.
20. Li, H.; Qu, Y.; Lu, J.; Li, S. A Composite Strategy for Harmonic Compensation in Standalone Inverter Based on Linear Active Disturbance Rejection Control. *Energies* **2019**, *12*, 2618. [CrossRef]
21. Barva, A.V.; Bhavsar, P.R. Design and Simulation of Four-leg Based Three-phase Four-wire Shunt Active Power Filter. In Proceedings of the International Conference on Communication information and Computing Technology (ICCICT), Mumbai, India, 2–3 February 2018.
22. Peng, F.Z.; Akagi, H.; Nabae, A. A New Approach to Harmonic Compensation in Power Systems-a combined System of Shunt Passive and Series Active Filters. *IEEE Trans. Ind. Appl.* **1990**, *26*, 983–990. [CrossRef]

23. Fujita, H.; Akagi, H. A Practical Approach to Harmonic Compensation in Power Systems-series Connection of Passive and Active Filters. *Ind. Appl.* **1991**, *27*, 819–829. [CrossRef]

24. Long, J.; Wu, J.; Liu, X.; Chen, S.; Chen, Z. Simulation and Design of Fast Charging and Discharging of Bi-directional DC-DC Converter for the Active Power Filter. *High Volt. Eng.* **2013**, *39*, 1792–1797.

25. Zhang, F.; Geng, Z.; Wei, Y. The algorithm of Interpolating Windowed FFT for harmonic analysis of electric power system. *IEEE Trans. Power Deliv.* **2001**, *16*, 160–164. [CrossRef]

26. Filipski, P. The Measurement of Distortion Current and Distortion Power. *IEEE Trans. Instrum. Meas.* **1984**, *33*, 36–40. [CrossRef]

27. Du, T.; Chen, G.; Lei, Y. A Novel Method for Power System Harmonic Detection Based on Wavelet Transform with Aliasing Compensation. *Proc. CSEE* **2005**, *25*, 54–59.

28. Peng, F.Z.; Lai, J.S. Generalized Instantaneous Reactive Power Theory for Three-phase Power Systems. *IEEE Trans. Instrum. Meas.* **1996**, *45*, 293–297. [CrossRef]

29. Liu, L.; Wei, X.; Ye, H. Measurement Method of Reactive Power Based on Instantaneous Reactive Power Theory. *Proc. CSU-EPSA.* **2017**, *29*, 121–125.

30. Emanuel, A.E.; Orr, J.A.; Cyganski, D.; Gulachenski, E.M. A Survey of Harmonic Voltages and Currents at Distribution Substations. *IEEE Trans. Power Deliv.* **2002**, *6*, 1883–1890. [CrossRef]

31. Luo, S. An Adaptive Detecting Method for Harmonic and Reactive Currents. *Trans. China Electrotech. Soc.* **1993**, *42*, 334–338.

32. Lu, J.; Savaghebi, M.; Guerrero, J.M.; Vasquez, J.C.; Xie, C. Linear Active Disturbance Rejection Control for LCL Type Grid-connected Converter. In Proceedings of the 42nd Annual Conference of the IEEE Industrial Electronics Society IECON, Florence, Italy, 23–26 October 2016; pp. 3458–3463.

33. Han, Z.; Shen, Z.; Gao, Z. An active disturbance rejection control solution for the two-mass-spring benchmark problem. In Proceedings of the American Control Conference, Boston, MA, USA, 6–8 July 2016.

34. Benrabah, A.; Xu, D.; Gao, Z. Active Disturbance Rejection Control of LCL-Filtered Grid-Connected Inverter Using Padé Approximation. *IEEE Trans. Ind. Appl.* **2018**, *54*, 6179–6189. [CrossRef]

35. Jin, H.; Song, J.; Lan, W.; Gao, Z. On The Characteristics Of ADRC: A PID Interpretation. *Sci. China Inf. Sci.* **2019**. [CrossRef]